

Simultaneous Enhancement of Upconversion and Downshifting Luminescence via Plasmonic Structure

Kyu-Tae Lee,^{†,§} Jong-Hyun Park,^{†,⊥} S. Joon Kwon,[†] Hyun-Keun Kwon,^{†,§} Jihoon Kyhm,[†] Kyung-Won Kwak,[¶] Ho Seong Jang,[†] Su Yeon Kim,[†] Joon Soo Han,[†] Sung-Hwan Lee,[†] Dong-Hun Shin,[†] Hyungduk Ko,[†] Il-Ki Han,[†] Byeong-Kwon Ju,^{*,§} Soong-Hong Kwon,^{*,¶} and Doo-Hyun Ko^{*,†,‡}

[†]Korea Institute of Science and Technology, Hwarang-ro, 14-gil, Seongbuk-gu, Seoul 136–791, Republic of Korea

[‡]Department of Applied Chemistry, Kyung Hee University, Yongin, Gyeonggi 130-701, Korea

[§]School of Electrical Engineering, Korea University, Anam-ro, Seongbuk-gu, Seoul 136–713, Republic of Korea

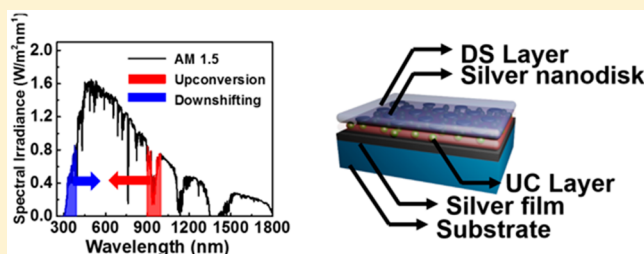
[⊥]Department of Chemistry, Korea University, Anam-ro, Seongbuk-gu, Seoul 136-701, Republic of Korea

[¶]Department of Chemistry and ^{||}Department of Physics, Chung-Ang University, Seoul 156-756, Korea

S Supporting Information

ABSTRACT: We describe a metal nanodisk–insulator–metal (MIM) structure that enhances lanthanide-based upconversion (UC) and downshifting (DS) simultaneously. The structure was fabricated using a nanotransfer printing method that facilitates large-area applications of nanostructures for optoelectronic devices. The proposed MIM structure is a promising way to harness the entire solar spectrum by converting both ultraviolet and near-infrared to visible light concurrently through resonant-mode excitation. The overall photoluminescence enhancements of the UC and DS were 174- and 29-fold, respectively.

KEYWORDS: Upconversion, downshifting, plasmonic structure, energy transfer, metal nanopattern, nanotransfer printing, solar spectrum conversion



Spectrum conversion materials that convert the ultraviolet (UV) and near-infrared (NIR) spectrum to the visible (VIS) spectrum have been investigated. The energy transition of light by lanthanide materials is particularly interesting because of the potential to overcome current limitations in photovoltaics,¹ bioimaging,^{2,3} and displays⁴ as a result of the materials' sharp fluorescence emission peaks, bright and monochromatic emissions, large Stokes/anti-Stokes shift, and extraordinarily long fluorescence lifetime.^{5–8} With respect to photovoltaics, the spectral mismatch between the energy band gap (E_g) of the photoactive layer and the photon energy distribution of the incident solar spectrum degrades device performance, that is, the transmissive loss of sub-band gap light ($E < E_g$) and the loss of excessive photon energy ($E > E_g$) via nonradiative relaxation.⁹ This discrepancy can be ameliorated by either transferring transmitted sub-band gap light to above-band gap light^{10,11} or shifting high-energy photons into lower-energy photons,¹² in which the spectral responsivity of the target solar cell can be matched (see Figure 1a); these transfer mechanisms by lanthanide-doped materials are denoted as upconversion (UC) and downshifting (DS), respectively. Owing to the potential advantages of energy transition materials in applications, many studies have attempted to improve their conversion efficiency. Energy transition has been enhanced by mainly two strategies: fabrication of efficient

conversion materials and photon management with nanostructures. Advances in UC have been achieved with the use of the lanthanide ions Yb^{3+} , Tm^{3+} , Ho^{3+} , and Er^{3+} , which act as sensitizers or activators for the UC process.^{13–17} Although the quantum efficiency of UC materials has been significantly improved,¹⁸ the materials still have intrinsic limitations such as relatively low absorption and emission efficiency, which in turn hinder the widespread use of UC materials as spectral converters.¹⁹ Recently, plasmonic structures with noble metals, in which the collecting efficiency of sensitizers is improved with the application of a local electric field near the metal structure, have been introduced to resolve these limitation issues.^{20–25} Electric field localization enhances absorption,^{26–28} improves the spontaneous emission rate,²⁹ and the energy transfer rate.³⁰ Recent studies have shown that coupling UC materials with metal nanostructures such as array of metallic nanostructures,^{31,32} metallic codoped nanocrystals,²³ and metal nanohole array³³ enables a straightforward amelioration in UC efficiency. Despite the theoretical and experimental expectations of these approaches, they have achieved only mild emission enhance-

Received: December 27, 2014

Revised: March 6, 2015

Published: March 10, 2015

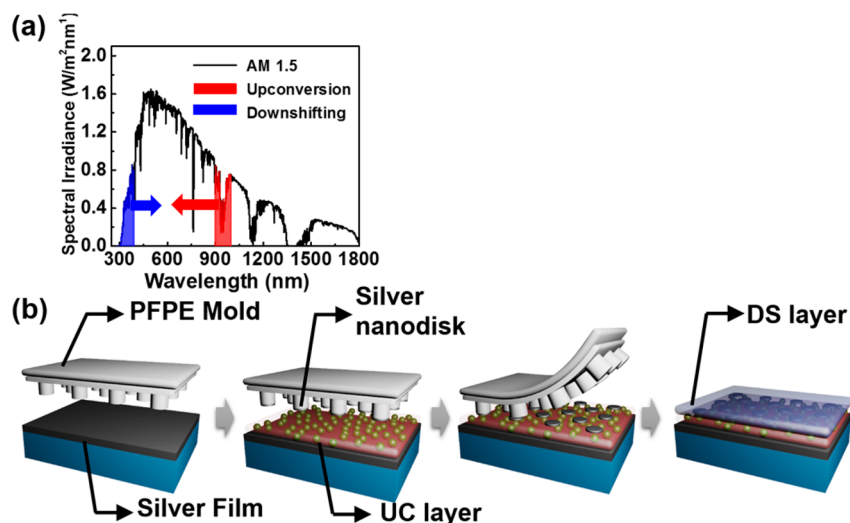


Figure 1. (a) Solar cell efficiency enhancement scheme using UC or DS material. The blue part reflects the energy transition from the UV region to the VIS region using a DS material, and the red part reflects the energy transition from the IR region to the VIS region using an UC material. (b) Schematic of the fabrication process using a nanoimprinting method for the metal nanopatterns.

ment for device application, and their fabrication in scalable areas is far from easy and is expensive. Besides, the focus has been on only half of the process, that is, the conversion of infrared (IR) light to VIS light. Therefore, it demands an advanced route that converts both UV light and IR light to VIS light such that the spectral mismatch between the incident solar spectrum and a photoactive material can be reduced.

In this study, we demonstrated controlled coupling of two different lanthanide codoped materials, $\text{NaYF}_4:\text{Yb}^{3+},\text{Er}^{3+}$ for UC and $\text{Tb}(\text{thd})_3$ (thd = 2,2,6,6-tetramethyl-3,5-heptanedione) for DS, with a gap plasmon using a metal nanodisk–insulator–metal film (MIM) structure to achieve enhanced UC and DS luminescence simultaneously (see Supporting Information for UC synthesis). A large electromagnetic (EM) enhancement has been obtained in this particular structure owing to the gap plasmonic effect.^{34–36} A lanthanide materials mixed perhydropolysilazane (PHPS) solution, which forms silica film with heat treatment,³⁷ was used to fabricate a UC or DS material-embedded SiO_2 composite layer to be an energy transfer layer, and a dielectric spacer to prohibit luminescence quenching, which occurs when there is direct contact of the conversion nanoparticles with metal.^{33,38} Spin-coating of composite solutions enables the fabrication of a scalable spectral converter with optimized optical parameters. The relatively simple process of forming silica film from a PHPS solution compared with the conventional vacuum process (e.g., chemical vapor deposition) shows the potential for its use in flexible devices.

To fabricate a MIM structure via a facile process, we used the nanotransfer printing technique via a PFPE (perfluoropolyether)-based stamp³⁹ (Figure 1b). A silver layer (200 nm) was deposited on a quartz substrate, and then the UC layer, prepared by spin-casting the synthesized $\text{NaYF}_4:\text{Yb}^{3+},\text{Er}^{3+}$ nanoparticles⁴⁰ in PHPS solution, was placed on the silver layer. A silver film (30 nm) was thermally deposited onto the nanopatterned PFPE stamp, which was then brought into contact with the nanoparticle-embedded film to transfer the silver nanodisk array under precisely controlled temperature, pressure, and time. Subsequent hydrolysis at 130 °C in water vapor was used to form the UC nanoparticle-embedded SiO_2 film with silver nanopatterns. Scanning electron microscopy (SEM) and transmission electron microscopy (TEM) con-

firmed that the UC nanoparticles (UCNPs) were dispersed uniformly inside the SiO_2 film (Figure 2a,b). To obtain

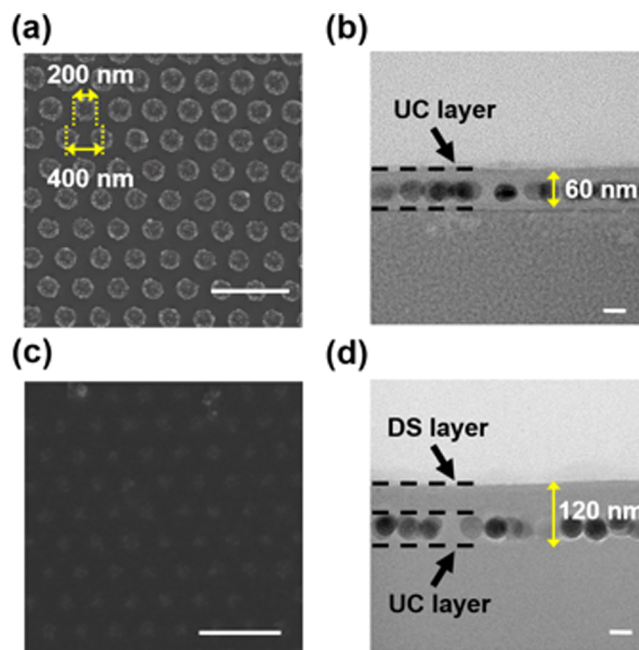


Figure 2. (a) Planar view of Ag nanoparticle array on the UC layer. (b) TEM image of the UC layer. (c) Planar view of the DS layer on the Ag nanoparticle array, which is on the UC layer. (d) TEM image of DS and UC layers. Scale bars: (a) 1 μm , (b) 30 nm, (c) 1 μm , (d) 30 nm.

simultaneous conversion of UV and IR light into VIS light, the DS material, $\text{Tb}(\text{thd})_3$, in PHPS solution was spin-coated on top of this metal patterned layer followed by hydrolysis in the oven at 130 °C (Figure 2c,d).

In principle, the design parameters of the MIM structure, that is, metal height, period, shape, and diameter, determine the plasmonic performance in the metal nanopatterns. The metal film in the MIM structure causes strong electric field localization by coupling with the upper metal nanopatterns.

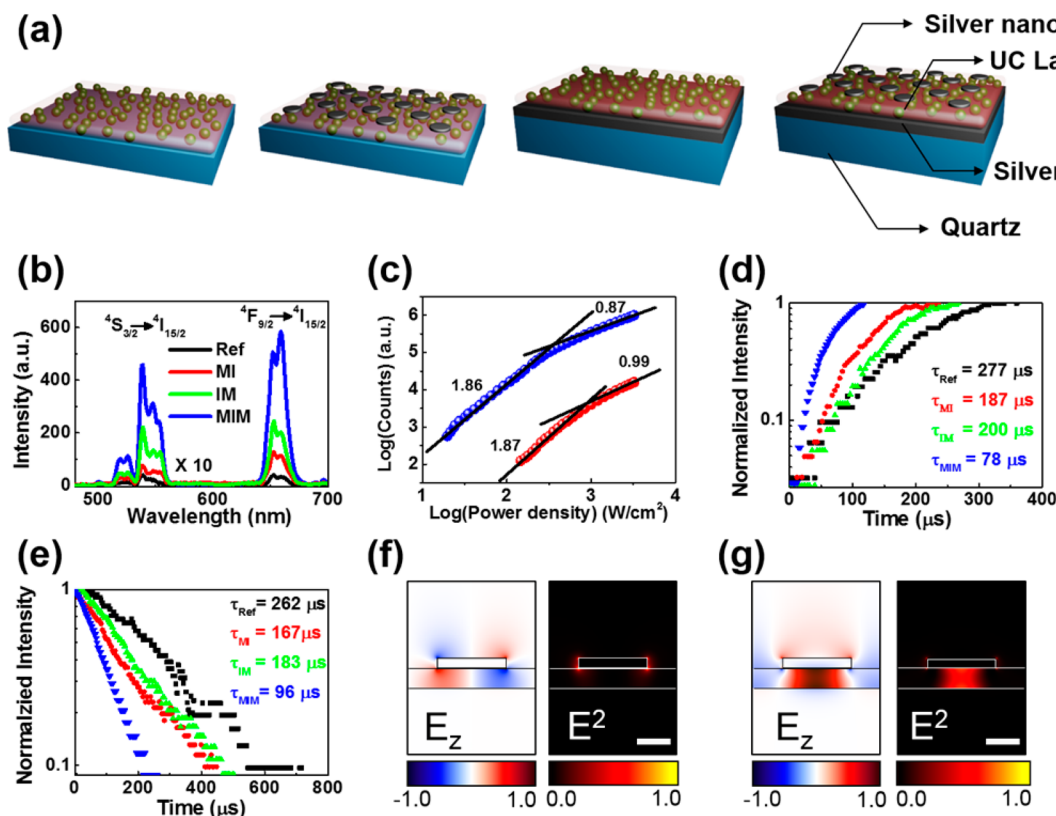


Figure 3. UC performance of the proposed structure and FDTD analysis. (a) UC structure series, including (from left to right) UC layer on a quartz substrate as the reference structure (ref), a metal pattern on ref (MI), UC layer on a metal substrate (IM), and a metal pattern on IM (MIM). (b) UC luminescence spectra of ref (black line), MI (red line), IM (green line), and MIM (blue line). The intensity of the spectra for MI, IM, and MIM are magnified 10-fold so that they are distinguishable. (c) Dependence of the UC luminescence intensity on the pump intensity for the ref (red sphere) and MIM (blue sphere) structures plotted on a double-logarithmic scale. (d) Rise time and (e) decay time of UC luminescence for the four UC structures at 659 nm emission under 970 nm excitation. Calculated mode profiles of MIM resonant mode excited near (f) absorption wavelength (970 nm) and (g) emission wavelength (549 nm and 659 nm) of UC layer. Scale bars for panels f and g are 100 nm.

We performed finite-difference time-domain (FDTD) calculations to obtain the optimum parameters of the MIM structure to enhance UC and DS luminescence simultaneously (see Supporting Information for the optimization of design parameters). The MIM structure consisted of a hexagonal array of metal (Ag) nanodisks, each 200 nm in diameter, 30 nm high, and with a translational periodicity of 400 nm. The UC layer between the metal (Ag) film and the nanodisk array was designed to be 60 nm thick, and the 60 nm thick DS layer uniformly covered the UC layer and the Ag nanodisk array (Figure 2 shows the MIM structure marked with its precise dimensions). We performed energy-dispersive X-ray spectroscopy (EDS) to certify the composition of the UC and DS layers (Supporting Information, Figures S6–S8).

First, we explored the UC process of the plasmonic nanostructures and the optical characteristics of the UC structure series, which consisted of an Ag nanodisk array, Ag film, and a UC material-embedded SiO₂ film (Figure 3a). The reference sample (ref) was prepared by depositing a UC layer on a quartz substrate. The Ag film between the substrate and the UC layer (denoted IM) was introduced to improve the extraction efficiency by reflecting the emitted light. To couple the UC layer and the metal pattern, the Ag nanodisk array on the UC layer (denoted MI) was formed using the previously described nanotransfer printing technique. Finally, to further boost the coupling effect in the form of a MIM structure, the Ag nanodisk array was transferred onto the IM structure

(denoted MIM).^{41,42} We chose these four structures to understand the principle behind UC luminescence. The plasmonic performance was investigated compared to the reference sample (ref). Under 970 nm laser excitation (see Supporting Information, Figure S9a for UC experimental setup), the UC luminescence exhibited peaks at 539 nm ($^2H_{11/2}/^4S_{3/2} \rightarrow ^4I_{15/2}$) and 659 nm ($^4F_{9/2} \rightarrow ^4I_{15/2}$) corresponding to the major transitions of light in the Er³⁺ state (Figure 3b). The UC luminescence for the MIM structure was observed to be strongly enhanced both at red (659 nm) and green (539 nm) emission under 318 W/cm² pumping power. In particular, the enhancement factors (EFs) for the red and green emission were 174 and 115, respectively (c.f., EFs for the MI and IM structures at the red emission were 3 and 6, respectively). It should be noted that the observed EFs for the red and green emission are closely correlated showing the same (two) orders of magnitude. This correlation tendency has also been observed in other UC-related system recently^{30,32,33,43–45} (refer to the relationship between the EFs for the green and the red emission for the UC luminescence provided in the Supporting Information). This luminescence enhancement was also seen when we measured the luminescence behavior of the UC structure series with an integrating sphere (Supporting Information, Figure S11).

The PL enhancement factor for the UC structure was characterized by various laser intensities. In a nonlinear process in the UC material, a certain number of pump photons is

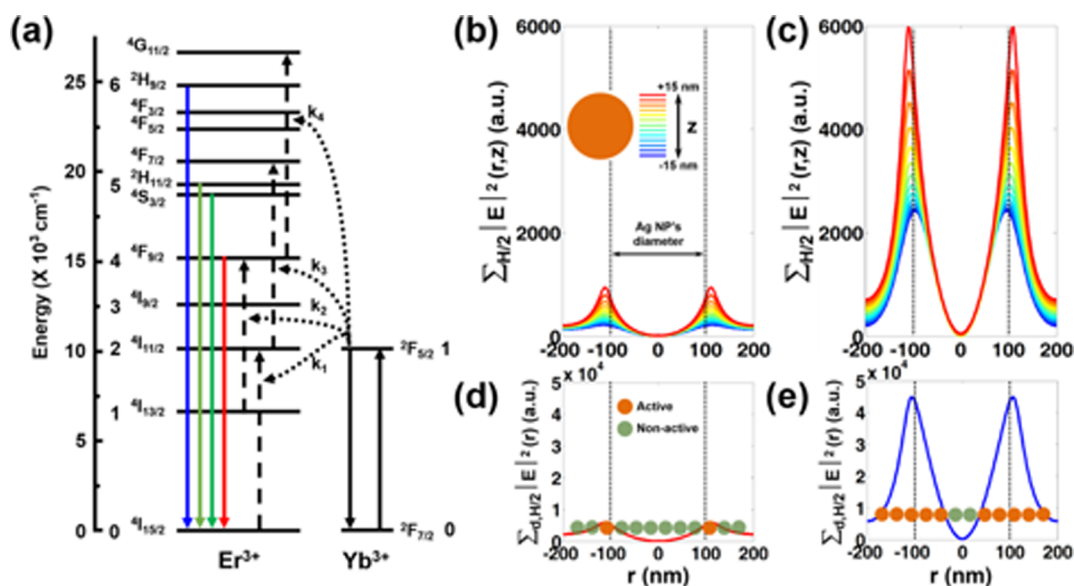


Figure 4. (a) Energy diagram of UC material (NaYF₄:Yb³⁺,Er³⁺) and comparison of the plasmonic effects of the MI and MIM structures simulated using the FDTD method. Distribution of the squared intensity of electromagnetic field in the x,y plane measured at different z positions (color-coded), $\sum_{H/2} |E|^2(r,z)$, for the (b) MI and (c) MIM structures, respectively. Vertical dotted lines guide the position of the top of the Ag nanoparticle (NP). Integrated $\sum_{H/2} |E|^2(r,z)$ over the z space occupied by the UC NPs, $\sum_{d,H/2} |E|^2(r)$, for the (d) MI and (e) MIM structures, respectively. Color-filled circles guide the array of the UC NPs (sized to scale) (blue for active and brown for nonactive under the plasmonic effect).

required to excite electrons to an emitting state. The slope of the UC luminescence intensity versus the pumping power density plotted on a double-logarithmic scale represents the number of photons involved in the energy transfer transition. The UC process reaches an order of two at a low power density and saturates to one when the power density is high because the population of the excited states is sufficiently large.⁴⁶ The slope is a function of the competition between linear decay and the UC process, which was described by Pollnau et al.⁴⁷ In our experiment, the UC luminescence intensity as a function of laser power density was measured at 659 nm and plotted on a double-logarithmic scale. The slope for each structure was analyzed by a linear fitting process (Figure 3c). The luminescence intensity of both the ref and MIM structures exhibited quadratic dependence on the power density below 250 W/cm², with a slope of approximately 1.86. On the other hand, the slope decreased to ~ 1 at power densities >1500 W/cm², which indicates that the linear decay process dominates. Therefore, our structures followed their intrinsic UC properties,⁴⁷ but the UC luminescence enhancement factor for the MIM structure became constant at power densities <250 W/cm².

The enhancement of UC luminescence results from improvements in absorption, emission, and energy transfer rate.^{33,48–54} To understand the large photoluminescence (PL) enhancement that occurs in the MIM structure, we performed absorption and emission enhancement calculations using the FDTD method. The large absorption enhancement originated from the enhancement of the electric field intensity of the normal incident light at 970 nm (Supporting Information, Figure S12). Figure 3, panel f demonstrates the plasmonic resonant MIM cavity mode at a wavelength of 970 nm, which induces a strong electric field in the UC layer. Because the resonant cavity mode can be excited efficiently by the pumping beam, the absorption can be enhanced. Time-resolved photoluminescence (TRPL) was measured to analyze the resonant plasmonic mode coupling at the excitation wave-

length; the coupling was indicated by the decrease in the rise time from 262 μ s for the ref to 96 μ s for the MIM, as seen in Figure 3, panel d.

Along with absorption enhancement in the pumping wavelength range, the FDTD calculations showed that the MIM structure is expected to enhance both the spontaneous emission rate and the extraction efficiency. The emission powers of the MIM and ref structures were obtained by placing a linearly polarized dipole at various positions of the UC layer and averaging the values. These values showed that there was considerable enhancement in the emission power, which was attributed to the MIM resonant cavity mode at the emission range (Figure 3g). The resonance modifies the spontaneous emission of a dipole via the Purcell effect^{55,56} and changes the direction of the emission into free space, where it is detected. This spontaneous emission enhancement in the MIM structure was observed as the decrease in the decay rate of the TRPL (Figure 3e), which was about three times faster than that of the ref structure. Detailed analysis of the TRPL showed that the radiative decay rate of the MIM structure at red emission wavelength (659 nm) was enhanced 22.62-fold compared to that of the ref structure (see Supporting Information for details). The Purcell factor was calculated to quantitatively analyze the large enhancement of PL emission. Interestingly, the increase in the calculated radiative decay rate was considerably greater than the calculated Purcell factor of 9.82. This indicates that the observed large enhancement of the PL emission is governed by a complicated mechanism along with the Purcell effect. In summary, the emission enhancement of the MIM system is the result of a combination of enhanced absorption efficiency, energy transfer rate, and plasmonic effects (see Supporting Information for details on the Purcell factor calculation).

To further explore additional mechanisms responsible for PL emission enhancement in the MIM structure, we adapted a rate-equation-based model^{30,54} in which steady-state electron densities at the donor and acceptor energy states are described

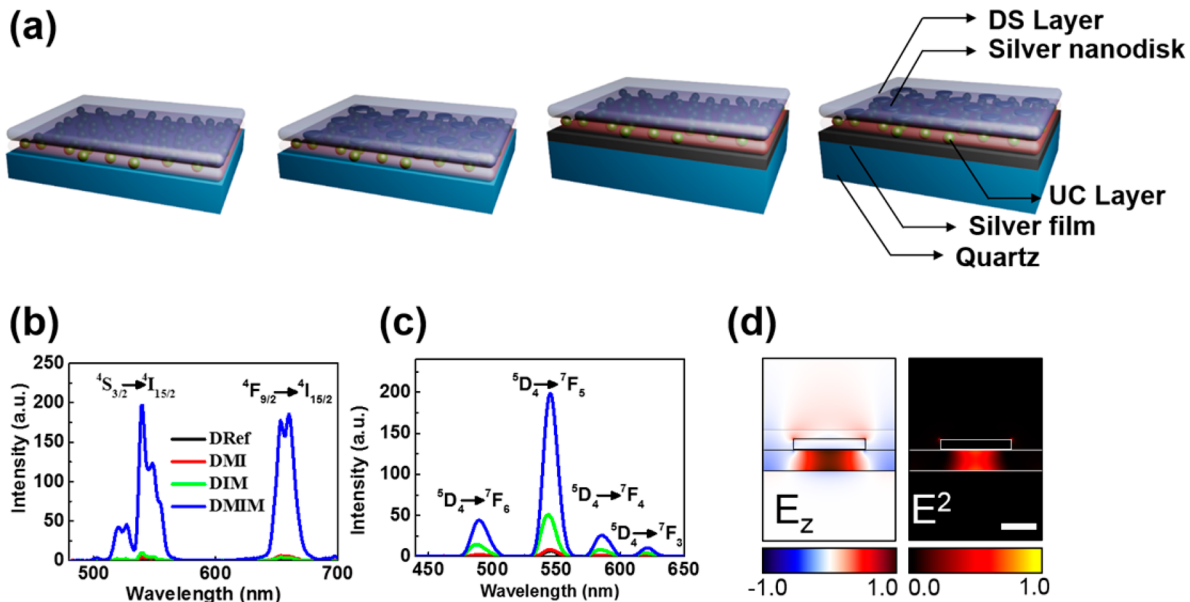


Figure 5. Optical properties and FDTD results of the UC and DS layers. (a) UC structure series with DS layer including (from left to right) DS layer on ref (DRef), metal pattern on DRef (DMI), DS layer on IM (DIM), and metal pattern on MIM (DMIM). (b) UC spectrum of DRef (black line), DMI (red line), DIM (green line), and DMIM (blue line). (c) DS spectrum of DRef (black line), DMI (red line), DIM (green line), and DMIM (blue line). (d) Calculated profiles of the MIM resonant mode at emission range. Scale bar for panel d is 100 nm.

in terms of energy transfer between states and radiative/nonradiative decay under continuous excitation conditions. Given continuously pumped excitation laser flux into the sample, I , we can assume that the kinetics governing the rate equation reached the steady state quickly. With further simplifications to the system and using applicable experimental conditions reported in the literature,^{30,54} we obtained the following rate equations at the steady state:

Acceptor energy levels (Er^{3+})

$$\text{Level 1: } 0 = W_{21}N_2 - k_2N_1n_1$$

$$\text{Level 2: } 0 = k_1N_0n_1 - k_3N_2n_1 - W_{21}N_2$$

$$\text{Level 4: } 0 = k_2N_1n_1 - W_{40}N_4$$

$$\text{Level 5: } 0 = k_3N_2n_1 - W_{50}N_5$$

Donor energy levels (Yb^{3+})

$$\text{Level 1: } 0 = fI\sigma n_0 - k_1N_0n_1 - k_2N_1n_1 - k_3N_2n_1$$

where N_i and n_j are the electron population densities at the acceptor energy level i and the donor energy level j , respectively; W_{ij} is the decay constant from the acceptor energy level i to level j ; radiative decay for $j = 0$ and nonradiative decay for $j > 0$; and k_i is the energy transfer coefficient from the acceptor energy level $i - 1$ to level i . For the donor energy level rate equation, f is the net fraction of flux that excites the electrons in the donor states, and σ is the absorption cross-section. Acceptor energy levels such as 3 and 6 were not included because their contributions to the entire set of dynamics are negligible (Figure 4a).

We obtained three distinguishable enhancement factors for PL emission from the PL intensities measured at green (539 nm) and red (659 nm) wavelengths, accompanied by the model parameters: (1) enhancement of absorption efficiency, (2) enhancement of energy transfer rate (k_1), and (3) an

increase in the fraction of the UCNPs affected by plasmonic resonance. Absorption efficiency is defined as the fraction of photoexcited Yb^{3+} , which acts as a medium for energy transfer to Er^{3+} , per unit influx of incident light. In this study, a comparison of the experimental data for the MI structure and the ref showed the dependence of f and k_1 on ϕ^* , the fraction of UCNPs under plasmonic resonance in the MI structure. UV-vis spectroscopy data on absorption enhancement showed that f and k_1 are enhanced 7.20- and 17.25-fold, respectively, at $\phi^* = 0.235$ for the MI structure. Combining the calculated enhancement factors demonstrates that the overall PL enhancement at the green and red emission wavelengths for the MIM structure is attributed to increases in f , k_1 , and ϕ (where ϕ is the fraction of UCNPs under plasmonic resonance in the MIM structure). To fix the value of ϕ , we compared the absorption enhancement factors of the MI and MIM structures by numerically integrating the square of the EM wave intensity in the structures $[\sum_{H/2}|E^2(r,z)|]$ (Figure 4b,c). The calculations showed that the plasmonic effect was enhanced 4.22-fold, which means that the MIM structure has a large plasmonic effect, whereas in the MI structure, only 23.5% of the UCNPs are affected by the plasmonic effect (i.e., $\phi = 4.22\phi^*$) (Figure 4d,e). Using the calculated value of $\phi = 0.991$, we found that f and k_1 are enhanced 20.35- and 18.70-fold, respectively, in the MIM structure compared to the ref. Thus, these factors account for the remaining mechanism responsible for the large enhancement of the PL emission along with the Purcell effect. From the analysis of UC processes, we found that our MIM structure exhibits improved energy transfer rate with stronger Purcell effect than the previous reported plasmonic structures^{30,57} such as linear, bullseye, pyramidal, and nanograting structures. In addition, nonradiative decay rates at the MIM structure (Supporting Information, Table S2) have decreased compared with those of the ref structure, which proves that quenching effect could be negligible in our MIM structures (further details are given in the Supporting Information).

The suggested MIM cavity mode was explored to enhance UC and DS luminescence simultaneously for a wide-spectrum conversion template approach. The DS layer was deposited by spin-casting the PHPS solution with $\text{Tb}(\text{thd})_3$ on the previous four UC structures. These new structures are called DRef, DMI, DIM, and DMIM (see Figure 5a for structure configuration). For efficient conversion, we placed the DS layer on top of the upconverter. This ensured that the short-wavelength light (UV) was absorbed by the upper DS layer, and the relatively long-wavelength light (NIR) reached the UC layer without significant loss. To confirm that the DS layer did not affect the luminescence of the UC layer, we repeated the experiments we conducted on the UC layer structure series. The PL enhancements for the four structures with a DS layer were similar to those of the UC-layer-only structures. Figure 5, panel b shows that the UC luminescence of DMI, DIM, and DMIM at 659 nm and 286.8 W/cm² pumping power was enhanced 2.7-, 1.7-, and 92-fold, respectively. This performance indicates that the existence of a DS layer still guarantees large enhancement of UC luminescence. Therefore, the DS layer above can be considered “transparent” in the NIR region.

DS luminescence was measured by exciting the structures with a 325 nm He–Cd gas laser (see Supporting Information, Figure S9b for DS experimental setup). Owing to the f – f internal orbital transition of Tb^{3+} , the radiative transitions from the $^5\text{D}_4$ level to the $^7\text{D}_{3,4,5,6}$ levels exhibit peaks at 489, 545, 586, and 621 nm, respectively (Figure 5c).⁵⁸ DMIM structure achieved an enhancement factor of 29 at 545 nm. The large enhancement of the DS luminescence originated from the strong resonant coupling with the MIM cavity mode. The spontaneous emission and extraction efficiency for the DMIM structure were greatly enhanced because the z -polarized dipole was resonantly coupled by the MIM cavity mode.

Our DMIM structure was carefully designed to enhance the electric field at both the downshifted and upconverted emission wavelengths. Here, the addition of a lanthanide conversion layer as a DS layer provided an advantage over other conversion materials because the emission is well matched with the UC emission from similar energy levels.^{59–61} Moreover, its large Stokes shift prohibits self-absorption in the DS layer^{62,63} and enables it to utilize short UV light by converting it into VIS light. Therefore, these advantages effectively increase both DS and UC luminescence. TRPL was measured to further confirm the DS performance of these structures. The decay time for the non-MIM structures, DMI, and DIM behaved in a similar manner, which indicated that the PL enhancement was due to scattering from the Ag nanodisk array or to reflection from the Ag film. In contrast, the decay time of the DMIM structure notably decreased by 56%, which supported the enhanced spontaneous rate for DMIM (Supporting Information, Figure S18). The FDTD calculations estimated that the DMIM structure exhibited a 29-fold enhancement of emission power compared with that of DRef, which was consistent with the measured PL performance.

In conclusion, we designed and fabricated a MIM structure that enhanced UC and DS luminescence simultaneously. The structure was created via a nanotransfer printing method that can fabricate a uniform structure across a large area. The easy fabrication of the proposed structure is an advantage for its use in flexible devices. The optimized Ag nanodisk array and conversion layer thickness of the structure matched the MIM resonance mode, which resulted in 174- and 29-fold enhancement of UC and DS luminescence, respectively. The lanthanide

luminescence layers enabled the use of the cavity mode to enhance luminescence by matching the emission ranges from UC and DS. This approach offers the possibility of harnessing the entire solar spectrum in photovoltaic devices.

■ ASSOCIATED CONTENT

§ Supporting Information

Quantitative analysis of the UC enhancement mechanism, EDS figures of materials, FDTD calculation results, experimental setup for TRPL measurements, additional figures, and synthesis scheme for UC nanoparticles. This material is available free of charge via the Internet at <http://pubs.acs.org>.

■ AUTHOR INFORMATION

Corresponding Authors

*E-mail: bkju@korea.ac.kr.

*E-mail: soonhong.kwon@gmail.com.

*E-mail: dhko@khu.ac.kr.

Author Contributions

K.-T.L. and J.-H.P. contributed equally to this work.

Notes

The authors declare no competing financial interest.

■ ACKNOWLEDGMENTS

This research was supported by the Pioneer Research Center Program through the National Research Foundation of Korea, which is funded by the Ministry of Science, ICT, and Future Planning (NRF-2013M3C1A3065040). It was also partly supported by a National Research Foundation of Korea grant (NRF-2009-C1AAA001-0092935), which is funded by the Ministry of Science, ICT, and Future Planning. We acknowledge support from grants of 2E25373 from KIST project.

■ REFERENCES

- (1) Deng, K.; Gong, T.; Hu, L.; Wei, X.; Chen, Y.; Yin, M. *Opt. Express* **2011**, *19*, 1749–1754.
- (2) Yi, G.; Lu, H.; Zhao, S.; Ge, Y.; Yang, W.; Chen, D.; Guo, L. H. *Nano Lett.* **2004**, *4*, 2191–2196.
- (3) Shen, J.; Sun, L. D.; Yan, C. H. *Dalton Trans.* **2008**, *24*, 5687–5697.
- (4) Downing, E.; Hesselink, L.; Ralston, J.; Macfarlane, R. M. *Science* **1996**, *273*, 1185–1189.
- (5) Georges, J. *Analyst* **1993**, *118*, 1481–1486.
- (6) Vetrone, F.; Capobianco, J. A. *Int. J. Nanotechnol.* **2008**, *5*, 1306–1339.
- (7) Yuan, J. L.; Wang, G. L. *Trends Anal. Chem.* **2006**, *25*, 490–500.
- (8) Binnemans, K. *Chem. Rev.* **2009**, *109*, 4283–4374.
- (9) Shockley, W.; Queisser, H. J. *J. Appl. Phys.* **1961**, *32*, 510–519.
- (10) Auzel, F. *Chem. Rev.* **2004**, *104*, 139–173.
- (11) Haase, M.; Schaefer, H. *Angew. Chem., Int. Ed.* **2011**, *50*, 5808–5829.
- (12) Wegh, R. T.; Donker, H.; Oskam, K. D.; Meijerink, A. *Science* **1999**, *283*, 663–666.
- (13) Krämer, K. W.; Biner, D.; Frei, G.; Güdel, H. U.; Hehlen, M. P.; Luthi, S. R. *Chem. Mater.* **2004**, *16*, 1244–1251.
- (14) Heer, S.; Kömpe, K.; Güdel, H.-U.; Haase, M. *Adv. Mater.* **2004**, *16*, 2102–2105.
- (15) Wang, F.; Liu, X. *Chem. Soc. Rev.* **2009**, *38*, 976–989.
- (16) Menyuk, N.; Dwight, K.; Pierce, J. W. *Appl. Phys. Lett.* **1972**, *21*, 159–161.
- (17) Wang, F.; Han, Y.; Lim, C. S.; Lu, Y.; Wang, J.; Xu, J.; Chen, H.; Zhang, C.; Hong, M.; Liu, X. *Nature* **2010**, *463*, 1061–1065.
- (18) Zou, W.; Visser, C.; Maduro, J. A.; Pshenichnikov, M. S.; Hummelen, J. C. *Nat. Photonics* **2012**, *6*, 560–564.

- (19) Boyer, J. C.; van Veggel, F. C. J. M. *Nanoscale* **2010**, *2*, 1417–1419.
- (20) Lu, Y. L.; Chen, X. B. *Appl. Phys. Lett.* **2009**, *94*, 193110.
- (21) Balushev, S.; Yu, F.; Miteva, T.; Ahl, S.; Yasuda, A.; Nelles, G.; Knoll, W.; Wegner, G. *Nano Lett.* **2005**, *5*, 2482–2484.
- (22) Ebbesen, T. W.; Lezec, H. J.; Ghaemi, H. F.; Thio, T.; Wolff, P. A. *Nature* **1998**, *391*, 667–669.
- (23) Schietinger, S.; Aichele, T.; Wang, H.-Q.; Nann, T.; Benson, O. H. *Nano Lett.* **2010**, *10*, 134–138.
- (24) Lindquist, N. C.; Nagpal, P.; Lesuffleur, A.; Norris, D. J.; Oh, S.-H. *Nano Lett.* **2010**, *10*, 1369–1373.
- (25) Zhang, W.; Ding, F.; Chou, S. Y. *Adv. Mater.* **2012**, *24*, OP236–OP241.
- (26) Kelly, K. L.; Coronado, E.; Zhao, L. L.; Schatz, G. C. *J. Phys. Chem. B* **2003**, *107*, 668–677.
- (27) Dulkeith, E.; Morteau, A. C.; Niedereichholz, T.; Klar, T. A.; Feldmann, J. *Phys. Rev. Lett.* **2002**, *89*, 203002.
- (28) Schuller, J. A.; Barnard, E. S.; Cai, W.; Jun, Y. C.; White, J. S.; Brongersma, M. L. *Nat. Mater.* **2010**, *9*, 193–204.
- (29) Yablonovitch, E. *Phys. Rev. Lett.* **1987**, *58*, 2059–2062.
- (30) Lu, D.; Cho, S. K.; Ahn, S.; Brun, L.; Summers, C. J.; Park, W. *ACS Nano* **2014**, *8*, 7780–7792.
- (31) Mertens, H.; Polman, A. *Appl. Phys. Lett.* **2006**, *89*, 211107.
- (32) Saboktakin, M.; Ye, X.; Oh, S. J.; Hong, S.-H.; Fafarman, A. T.; Chettiar, U. K.; Engheta, N.; Murray, C. B.; Kagan, A. C. *ACS Nano* **2012**, *6*, 8758–8766.
- (33) Saboktakin, M.; Ye, X.; Chettiar, U. K.; Engheta, N.; Murray, C. B.; Kagan, A. C. *ACS Nano* **2013**, *7*, 7186–7192.
- (34) Hill, R. T.; Mock, J. J.; Urzhumov, Y.; Sebba, D. S.; Oldenburg, S. J.; Chen, S. Y.; Lazarides, A. A.; Chilkoti, A.; Smith, D. R. *Nano Lett.* **2010**, *10*, 4150–4154.
- (35) Lassiter, J. B.; McGuire, F.; Mock, J. J.; Ciraci, C.; Hill, R. T.; Wiley, B. J.; Wiley, A.; Smith, D. R. *Nano Lett.* **2013**, *13*, 5866–5872.
- (36) Chu, Y.; Banaee, M. G.; Crozier, K. B. *ACS Nano* **2010**, *4*, 2804–2810.
- (37) Kozuka, H.; Nakajima, K.; Uchiyama, H. *ACS Appl. Mater. Interfaces* **2013**, *5*, 8329–8336.
- (38) Feng, A. L.; You, M. L.; Tian, L.; Singamaneni, S.; Liu, M.; Duan, Z.; Lu, T. J.; Xu, F.; Lin, M. *Sci. Rep.* **2015**, *5*, 7779.
- (39) Niskala, J. R.; You, W. *J. Am. Chem. Soc.* **2009**, *131*, 13202–13203.
- (40) Na, H.; Woo, K.; Lim, K.; Jang, H. S. *Nanoscale* **2013**, *5*, 4242–4251.
- (41) Schuller, J. A.; Barnard, E. S.; Cai, W.; Jun, Y. C.; White, J. S.; Brongersma, M. L. *Nat. Mater.* **2010**, *9*, 193–204.
- (42) Khatir, M.; Granpayeh, N. *IEEE Trans. Magn.* **2013**, *49*, 1343–1352.
- (43) Deng, W.; Sudheendra, L.; Zhao, J.; Fu, J.; Jin, D.; Kennedy, I. M.; Goldys, E. M. *Nanotechnology* **2011**, *22*, 325604.
- (44) Liao, J.; Yang, Z.; Lai, S.; Shao, B.; Li, J.; Qiu, J.; Song, Z.; Yang, Y. *J. Phys. Chem. C* **2014**, *118*, 17992–17999.
- (45) Yuan, P.; Lee, Y. H.; Gnanasammandhan, M. K.; Guan, Z.; Zhang, Y.; Xu, Q. *Nanoscale* **2012**, *4*, 5132–5137.
- (46) Suyver, J. F.; Aebischer, A.; García-Revilla, S.; Gerner, P.; Güdel, H. U. *Phys. Rev. B* **2005**, *71*, 125123.
- (47) Pollnau, M.; Gamelin, D. R.; Lüthi, S. R.; Güdel, H. U.; Hehlen, M. P. *Phys. Rev. B* **2000**, *61*, 3337–3346.
- (48) Atre, A. C.; Etxarri, A. G.; Alaeian, H.; Dionne, J. A. *J. Opt.* **2012**, *14*, 024008.
- (49) Zhang, H.; Li, Y.; Ivanov, I. A.; Qu, Y.; Huang, Y.; Duan, X. *Angew. Chem.* **2010**, *122*, 2927–2930.
- (50) Zia, R.; Schuller, J. A.; Chandran, A.; Brongersma, M. L. *Mater. Today* **2006**, *9*, 20–27.
- (51) Polman, A.; Atwater, H. A. *Mater. Today* **2005**, *8*, 56.
- (52) Lu, D.; Cho, S. K.; Ahn, S.; Brun, L.; Summers, C. J.; Park, W. *ACS Nano* **2014**, *8*, 7780–7792.
- (53) Wu, D. M.; Etxarri, A. G.; Salleo, A.; Dionne, J. A. *J. Phys. Chem. Lett.* **2014**, *5*, 4020–4031.
- (54) Sun, Q. C.; Munderoor, H.; Ribot, J. C.; Singh, V.; Smalyukh, I. I.; Nagpal, P. *Nano Lett.* **2014**, *14*, 101–106.
- (55) Kuttge, M.; Garcia de Abajo, F. J.; Polman, A. *Nano Lett.* **2010**, *10*, 1537–1541.
- (56) Akselrod, G. M.; Argyropoulos, C.; Hoang, T. B.; Ciraci, C.; Fang, C.; Huang, J.; Smith, D. R.; Mikkelsen, M. H. *Nat. Photonics* **2014**, *8*, 835–840.
- (57) Sun, Q.-C.; Casamada-Ribot, J.; Singh, V.; Munderoor, H.; Smalyukh, I. I.; Nagpal, P. *Opt. Express* **2014**, *22*, 11516–11527.
- (58) Kang, X.; Li, C.; Cheng, Z.; Ma, P.; Hou, Z.; Lin, J. *WIREs Nanomed. Nanobiotechnol.* **2014**, *6*, 80–101.
- (59) Johnson, N. J.; Sangeetha, N. M.; Boyer, J. C.; van Veggel, F. C. *Nanoscale* **2010**, *2*, 771–777.
- (60) Jacobs, R. R.; Krupke, W. F. *Appl. Phys. Lett.* **1979**, *34*, 497–500.
- (61) Shuvaev, S.; Utochnikova, V.; Marciniak, L.; Freidzon, A.; Sinev, I.; van Deun, R.; Freire, R. O.; Zubavichus, Y.; Grünert, W.; Kuzmina, N. *Dalton Trans.* **2014**, *43*, 3121–3136.
- (62) Terai, T.; Kikuchi, K.; Iwasawa, S.; Kawabe, T.; Hirata, Y.; Urano, Y.; Nagano, T. *J. Am. Chem. Soc.* **2006**, *128*, 6938–6946.
- (63) Eliseeva, S. V.; Bünzli, J.-C. G. *Chem. Soc. Rev.* **2010**, *39*, 189–227.